

High-Efficiency Resonant Beam Charging and Communication

Yunfeng Bai, *Student Member, IEEE*, Qingwen Liu, *Senior Member, IEEE*,

Xin Wang, *Senior Member, IEEE*,

Bin Zhou and Zhiyong Bu

Abstract

Simultaneous wireless information and power transfer (SWIPT) has been envisioned as an enabling technology for future 6G by providing high-efficiency power transfer and high-rate data transmissions concurrently. In this paper, we propose a resonant beam charging and communication (RBCC) system utilizing the telescope internal modulator (TIM) and the semiconductor gain medium. TIM can concentrate the diverged beam into a small-size gain module, thus the propagation loss is reduced and the transmission efficiency is enhanced. Since the semiconductor gain medium has better energy absorption capacity compared with the traditional solid-state one, the overall energy conversion efficiency can be improved. We establish an analytical model of this RBCC system for SWIPT and evaluate its stability, output energy, and spectral efficiency. Numerical analysis shows that the proposed RBCC system can realize stable SWIPT over 10 meters, whose energy conversion efficiency is increased by 14 times compared with the traditional system using the solid-state gain medium without TIM, and the spectrum efficiency can be above 15 bit/s/Hz.

Index Terms

Simultaneous Wireless Information and Power Transfer; Resonant Beam; Semiconductor Gain Medium; Telescope

Y. Bai, and Q. Liu, are with the College of Electronics and Information Engineering, Tongji University, Shanghai, China, (email: baiyf@tongji.edu.cn, qliu@tongji.edu.cn).

Xin Wang is with the Key Laboratory for Information Science of Electromagnetic Waves (MoE), Department of Communication Science and Engineering, Fudan University, Shanghai 200433, China (e-mail: xwang11@fudan.edu.cn).

B. Zhou, and Z. Bu, are with the Key Laboratory of Wireless Sensor Network and Communications, Shanghai Institute of Microsystem and Information Technology, Chinese Academy of Sciences, Shanghai, China, (email: bin.zhou@mail.sim.ac.cn, zhiyong.bu@mail.sim.ac.cn).

I. INTRODUCTION

In the era of 5G and beyond, network capacity will continue to increase for rapidly growing number of devices [1]. At the same time, the energy consumption of mobile devices is also increasing dramatically to support high-performance communication and computation [2]. Facing these demands, various technologies have been promoted, e.g., millimeter-wave transmission, ultra-dense cloud radio access networks, and massive multiple-input multiple-output (M-MIMO) arrays, etc. [3], [4]. In terms of energy consumption, wireless power transfer (WPT) for providing unlimited energy supply is undoubtedly one of the most attractive solutions [3]–[5]. Compared with wired power supply, WPT is flexible and suitable for mobile devices; compared with battery, WPT is not restricted by battery's capacity, weight, or volume [6], [7].

Simultaneous wireless information and power transfer (SWIPT) technology has attracted great attention from researchers to address the above issues. SWIPT technology is divided into two types: wide-beam broadcast and narrow-beam orientation. Wide-beam broadcast can support wide-coverage [8]. However, it faces the difficulty of achieving high-power transmission due to energy dissipation. Narrow-beam orientation technology such as laser or beamforming can support high-power transmission; however, the narrow beam leads to the challenge of positioning mobile receivers [9]. To meet the requirements of both high-power and mobility, resonant beam system (RBS) was proposed for SWIPT [10]. The resonant beam carries the optical signal cyclically in the resonant cavity which transfers energy and information between the transmitter and the receiver. Due to the energy concentration characteristics, RBS can achieve high power transfer [11]. By cooperating retro-reflectors, RBS enables self-alignment between the transmitter and the receiver for mobile SWIPT [12].

Since the light beam is the signal carrier in the RBS, the available bandwidth is larger than that of radio-frequency systems, which allows high-rate data transfer [13]. In addition, the light has no interference with radio frequency and thus the RBS is environmental-friendly [14]. What's more, when the line of sight (LoS) between the transmitter and the receiver is blocked due to the intrusion of foreign objects, the cyclic reciprocating process of the resonant beam in the cavity is interrupted immediately. This prevents foreign objects from continuous radiative exposure, thus ensures safety [15].

Due to these remarkable advantages, the RBS has been applied in various SWIPT applications such as unmanned aerial vehicles (UAV), smartphones, laptops, etc. [16], [17]. The theoretical

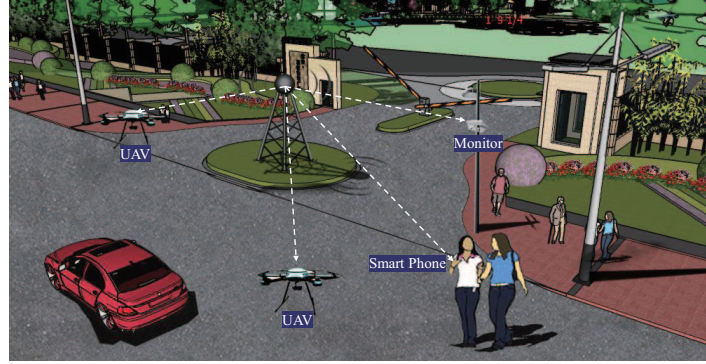


Fig. 1. Application scenarios of SWIPT

model, system design, network deployment of the RBS have been studied in the literature. Zhang *et al.* in [10] first presented the principle and establish the analysis model of the RBS for energy transfer (a.k.a. distributed laser charging). In addition to the theoretical analysis, Zhang *et al.* verified that the energy transfer of the RBS using solid-state gain medium can achieve 2W power transfer over 2.6m in experiment [11]. To support multiuser access into the RBS, Xiong *et al.* proposed a time-division multiple access (TDMA) RBS design for wireless power transfer [18]. Xiong *et al.* also proposed the RBS communication design and presented the analytical model in [19]. Liu *et al.* proposed the basic SWIPT model of the RBS and demonstrated its mobility using the retro-reflectors [12]. To evaluate the safety of the RBS, Fang *et al.* proposed an analytical model based on electromagnetic field analysis and assessed its safety with external object invasion [15].

Although the above studies explain the principle of RBS for SWIPT, both the energy conversion efficiency and transmission distance are limited. Due to conversion and transmission loss, the existing RBS schemes can only achieve the transmission distance up to a few meters and the conversion efficiency of around 1% [11]. In this paper, we propose an RBS design using the telescope internal modulator (TIM) and the semiconductor gain medium. Specifically, TIM can concentrate the diverged light beam into the small-sized gain module, thus reduce the transmission loss, and increase the transmission efficiency. In order to enhance energy conversion efficiency, the semiconductor gain medium is introduced to replace the solid-state one. Compared with the solid-state gain medium, the semiconductor has better energy absorption capability from the pump source. Thus, the energy level transition and population inversion efficiency are enhanced, threshold power decreases, and the overall conversion efficiency is improved.

The contributions of this paper are summarized as follows:

- We propose a resonant beam system design for SWIPT with enhanced transmission distance and conversion efficiency by adopting the telescope internal module (TIM) and the semiconductor gain medium.
- We present an analytical model of the proposed system, which describes the cavity stability, the beam propagation characteristics, the power output, the energy conversion efficiency, and data transfer capability.
- We evaluated the energy and data transfer performance efficiency relying on the proposed analytical model, which demonstrates that the energy conversion efficiency gains 14 times and the spectrum efficiency can be above 15bit/s/Hz.

The rest of the paper is organized as follows. In Section II, the model of the high-efficiency RBS involving the TIM and the semiconductor gain medium is described. In section III, the numerical evaluation of the system performance is depicted. In section IV, the conclusion is presented.

II. SYSTEM MODEL

A. System Structure

The system structure is shown in Fig. 2 . The system is divided into three parts: transmitter, receiver, and free space cavity. The transmitter is mainly composed of a gain module and a pump source. The pump source releases energy carrying the data signal in the form of optical radiation to the gain module. Then, with the function of optical radiation, the gain module occurs the stimulated absorption, spontaneous emission, and stimulated emission, which builds the basis of resonant beam generation. The receiver mainly includes two parts: photovoltaic (PV) panel module and avalanche photodiode (APD) module [20], [21]. The PV module converts light beam energy into electrical power. The APD module is used to detect the data signal. The free space cavity is composed of a reflector M1, a TIM, and a reflector M2. Among them, M1 and M2 constitute the resonant cavity. The photons generated on the gain module will oscillate back and forth within the cavity which will finally form the resonant beam. The TIM is placed on the optical path in front of the gain. It is used to change the phase of the incident resonant beam. Incident beam will be compressed by TIM before entering the gain, which can promote the beam incidence.

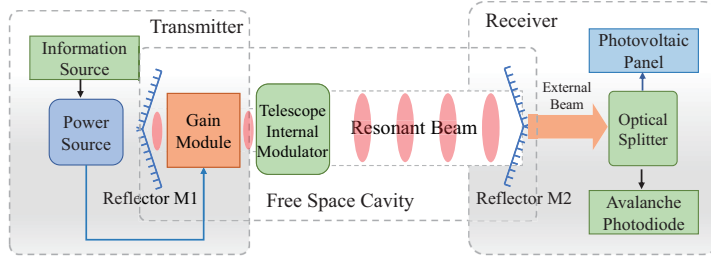


Fig. 2. High-efficiency resonant beam SWIPT system

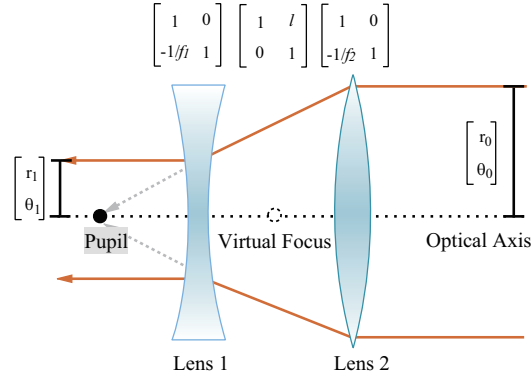


Fig. 3. Telescope internal modulator structure

B. Telescope Internal Modulator Model

The TIM structure consists of a concave lens and a convex lens that are placed in parallel and the center of the lens is collinear. The focal lengths of the concave lens and the convex lens are f_1 and f_2 . To make parallel incident light beams emerge in parallel, the focus of the convex lens in the direction of the concave lens coincides with the negative focus of the concave lens in the same direction to form an afocal optical system, that is, the relative distance of the two lenses satisfies [22]:

$$l = f_1 + f_2. \quad (1)$$

After the incident cavity beam passes through the convex lens, the convex lens adjusts the beam phase converging the beam to the focal point. Then, through the reverse phase correction of the concave lens, the beam passes the concave lens and form a compressed beam. Two main tasks have been completed in the above process: 1) beam compression; 2) beams emitted in parallel.

In order to define and analyze the transmission of light beams in space, We introduce the

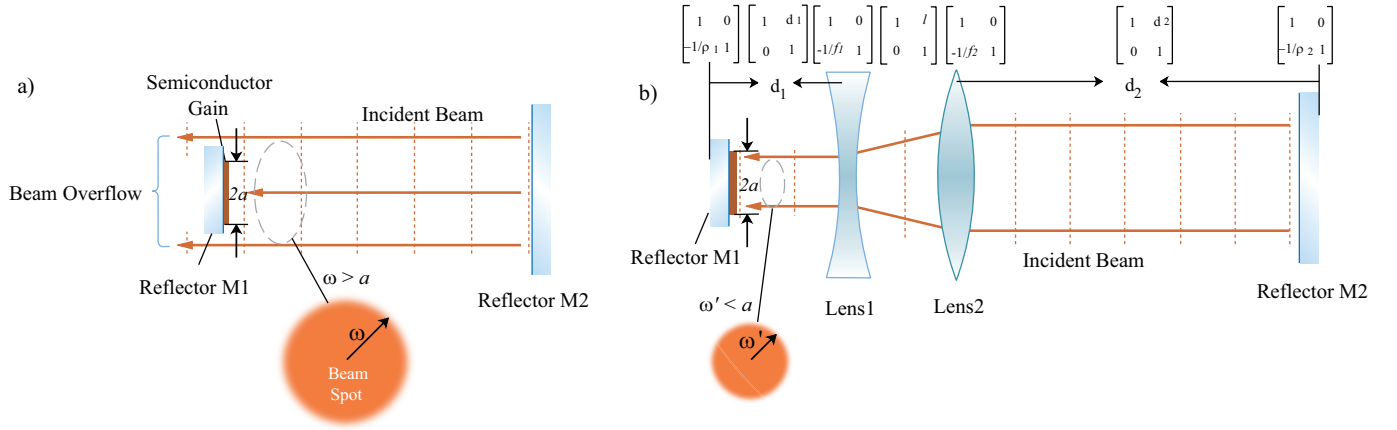


Fig. 4. Cavity structure characteristics of different RB system: a) original system without TIM, incident beam spot $\omega > a$; b) proposed system with TIM, incident beam spot $\omega' < a$

vector and matrix to accurately and strictly analyze the beam's transfer and change. In this time, the beam of light transfer under the paraxial approximation can be defined as [23], [24]:

$$\begin{bmatrix} r_i \\ \theta_i \end{bmatrix} = \mathbf{M}_0 \begin{bmatrix} r_0 \\ \theta_0 \end{bmatrix}. \quad (2)$$

where r_0 and r_i are the location parameter of the incident beam and the emergent beam, θ_0 and θ_i express the direction angle, and \mathbf{M}_0 is the transmission matrix.

Furthermore, if the beam passes through a series of optical components, the entire transmission matrix is a single matrix of these components multiplied in the corresponding order. For the proposed TIM structure shown in Fig. 3, the beam transmission matrix \mathbf{M}_T describes the beam passing through the free space to the lens 1, passing through lens 1 and free space with distance l , reaching lens 2, and finally passing through lens 2 into the free space again. These process can be expressed by matrix as:

$$\begin{aligned} \mathbf{M}_T &= \begin{bmatrix} 1 & 0 \\ -\frac{1}{f_2} & 1 \end{bmatrix} \begin{bmatrix} 1 & l \\ 0 & 1 \end{bmatrix} \begin{bmatrix} 1 & 0 \\ -\frac{1}{f_1} & 1 \end{bmatrix} \\ &= \begin{bmatrix} \frac{f_2-l}{f_2} & l \\ \frac{l-f_1-f_2}{f_1 f_2} & \frac{f_1-l}{f_1} \end{bmatrix}. \end{aligned} \quad (3)$$

f_1 and f_2 is the focal length of the lens1 and lens2; l expresses the transmission with the free space between the lenses. Since $l = f_1 + f_2$ for the TIM, the equation (3) will become

$$\mathbf{M}_T = \begin{bmatrix} -\frac{f_1}{f_2} & l \\ 0 & -\frac{f_2}{f_1} \end{bmatrix}. \quad (4)$$

To evaluate the beam adjustment of TIM, we introduce $M = -f_2/f_1$ as the TIM structure parameter.

C. Stable Cavity Model and Beam Spot Model

To achieve reliable and durable SWIPT, the resonant cavity needs to keep stable. At this time, the cavity can restrict the resonant beam overflow and limit the beam to travel back and forth between the transmitter and receiver [25], [26].

To obtain the stability conditions of the cavity, we need to define the propagation process of resonant beam in the cavity at first. Taking M1 as the starting point, the beam propagating in the cavity will pass through lens 1, lens 2, and reflector M2 in sequence. Free space is used as a medium between these components. We still use the matrix to express those process which is:

$$\begin{aligned} \mathbf{M}_c &= \mathbf{M}_{M2} \mathbf{M}_{d_2} \mathbf{M}_{L2} \mathbf{M}_1 \mathbf{M}_{L1} \mathbf{M}_{d_1} \mathbf{M}_{M1} \\ &= \begin{bmatrix} 1 & 0 \\ -\frac{1}{\rho_2} & 1 \end{bmatrix} \begin{bmatrix} 1 & d_2 \\ 0 & 1 \end{bmatrix} \begin{bmatrix} 1 & 0 \\ -\frac{1}{f_2} & 1 \end{bmatrix} \begin{bmatrix} 1 & l \\ 0 & 1 \end{bmatrix} \\ &\quad \begin{bmatrix} 1 & 0 \\ -\frac{1}{f_1} & 1 \end{bmatrix} \begin{bmatrix} 1 & d_1 \\ 0 & 1 \end{bmatrix} \begin{bmatrix} 1 & 0 \\ -\frac{1}{\rho_1} & 1 \end{bmatrix}, \end{aligned} \quad (5)$$

where \mathbf{M}_{M1} , \mathbf{M}_{M2} , \mathbf{M}_{L1} , and \mathbf{M}_{L2} express the matrix of reflector M1, M2 with curvature ρ_1 and ρ_2 , and lens L1, L2 with focal length f_1 and f_2 . \mathbf{M}_{d_1} , \mathbf{M}_{d_2} , and \mathbf{M}_1 express the beam transfer in the free space with distances d_1 , d_2 and l . Through matrix calculation, we can get the specific expression of matrix \mathbf{M}_c :

$$\begin{aligned} \mathbf{M}_c &= \begin{bmatrix} M - (d_1 M + d_2/M + l)/\rho_1 \\ d_1 M + d_2/M + l \\ ((L''/\rho_2 - 1)/M + (L'M)/\rho_2)/\rho_1 - M/\rho_2 \\ \frac{1}{M} - (d_1 M + d_2/M + l)/\rho_2 \end{bmatrix} \\ &= \begin{bmatrix} A & B \\ C & D \end{bmatrix}, \end{aligned} \quad (6)$$

where $L' = d_1 - f_1$ and $L'' = d_2 - f_2$.

According to [25] and (6), the system can keep stable when the elements of \mathbf{M}_c satisfy

$$0 < \left(M - \frac{l + d_1 M + d_2/M}{\rho_1} \right) \cdot \left(\frac{1}{M} - \frac{l + d_1 M + d_2/M}{\rho_2} \right) < 1. \quad (7)$$

The reflector M1 and M2 can reflect the incident light back from the original path. The reflector M1 is composed of a flat multilayer reflective medium, which means the curvature of M1 $\rho_1 = \infty$. At this time, the (7) can be simplified as:

$$0 < 1 - \frac{(f_1 - f_1 M) M + d_1 M^2 + d_2}{\rho_2} < 1. \quad (8)$$

From (8), we know that the stable cavity condition of the RB system changes with different parameters M, d_1, d_2, f_1 and ρ_2 . Among them, M, d_1, f_1 and ρ_2 are system structure parameters, and d_2 is the environmental variable which expresses the space distance between the transmitter and receiver. Therefore, through the stable cavity inequality, we can get: a) the variation range of the system's transmission distance d_2 at different system structure parameters, and b) the relationship between the structure parameters when the d_2 is determined.

Beam spot is the intensity distribution of the beam in the vertical propagation direction, and its radius is usually used to evaluate the lateral amplitude of the beam at a certain point. Based on [24], [25], when the cavity is under stable condition, the beam spot radius on the incident section of the gain module can be given by:

$$\omega_1^4 = - \left(\frac{\lambda}{\pi} \right)^2 \frac{BD}{AC}, \quad (9)$$

where ω_1 represents the beam mode radius on the gain module; A, B, C , and D are the matrix elements of \mathbf{M}_C mentioned above; λ is the wavelength of the resonant beam. The transmission loss is the main factor limiting the system transmission performance, which comes from the beam divergence, diffraction, and the mismatch between the beam and the elements' geometric boundary [27]. As shown in Fig. 4(a), when the light is reflected from the receiving end back to the transmitting end, beam divergence generates after long-distance transmission causing the beam spot radius $\omega > a$ (geometric radius of gain module), which leads to part of the beam overflow and diffract on the edge of the gain module, resulting in energy loss. Compared with the original system, the system scheme in Fig. 4(b) introduces the TIM. The divergent resonant beam is modulated and compressed by the TIM before entering the gain module ($\omega' < a$), which

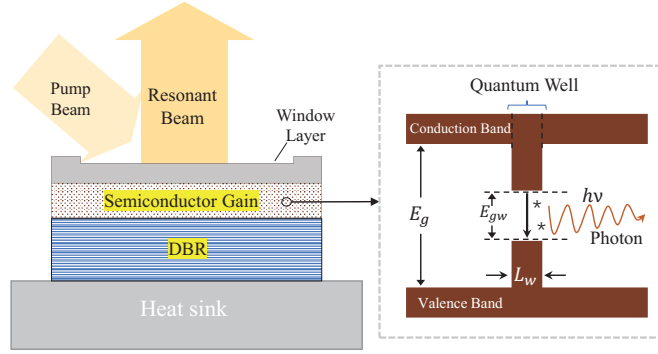


Fig. 5. Receiver structure and operating principles of the semiconductor gain

ensures entering effectively. Transmission loss caused by diffraction will be suppressed and the system's transmission distance will be increased.

D. Beam Energy Generation Model

According to Fig. 2, the oscillator cavity is mainly composed of reflectors M1, M2, TIM, and gain module. Among them, TIM consists of two lenses with high transmittance, whose absorption loss to the incident beam can be considered as 0. The radiation beam at any point propagates back and forth in the cavity will pass through these components, experiencing loss and gain. During this process, after one cycle, if the beam returns to the origin point and its energy is unchanged, we can conclude that the system achieves the balance of loss and gain. This equilibrium condition is called a threshold condition. Since the reflectivity of the mirrors M1 and M2 are R_1 and R_2 and the length of the gain module is h , the threshold condition can be expressed as [23], [28]:

$$R_1 R_2 T_{loss} \exp 2gh = 1, \quad (10)$$

where g represents the gain coefficient per unit length of the gain medium. Each time the beam travels through the gain, the beam energy intensity will increase by $\exp(gh)$ times. R_1 and R_2 can think as the beam emission ratio of M1 and M2. Normally, the value of R_1 is close to 1, and the value of R_2 changes according to the requirements of the output power. Energy losses such as the absorption dispersion of reflectors and air, internal loss per unit length in the gain, etc. are represented by T_{loss} .

Under the beam compression of the TIM, the resonant beam can effectively enter the size-limited gain module, which makes the micron-level semiconductor gain medium can be applied

in the system. Semiconductor gain utilizes the recombination of electrons in the conduction band and holes in the valence band to generate simulated radiation [29]. Compared with the solid gain medium, it has the following characteristics: 1) The active area and the cladding materials on both sides (window layer and distributed bragg reflector (DBR)) have a band-gap difference forming a potential barrier. It will confine electrons and holes within the active area, which is conducive to the recombination of electrons and holes; 2) The active area and the cladding materials have a refractive index difference. When photons transfer on the material boundary, they will be reflected back to the active area. The light field is restricted to the active area, which causes more stimulated radiation; 3) The gain medium has a hetero-junction quantum well structure. This structure (Fig. 5) can further reduce the thickness of the active layer to the nano-level producing the quantum effect. It makes the limitation of carriers and light fields be further strengthened and the forbidden bandwidth reduce from E_g to E_{gw} [30], [31]. Based on these characteristics, the loss of the particle conversion in semiconductor gain can be quite small, and the threshold value is also greatly reduced.

We use the small signal material gain coefficient g_0 , transparency carrier density N_0 , and the unit length gain coefficient g above to express the threshold carrier density N_{th} [32]:

$$N_{th} = N_0 \exp(g/g_0). \quad (11)$$

Among these parameters, N_0 and g_0 are material constant. Further, threshold P_{th} can be expressed by [32]:

$$P_{th} = N_{th} \frac{EhA_p}{\eta_{abs}\tau_{N_{th}}}, \quad (12)$$

where $h = N_w \cdot L_w$, η_{abs} expresses the pump absorption efficiency, E is photon energy, $A_p = \pi(d_{pump}/2)^2$ is the effective pump area, and $\tau_{N_{th}}$ is carrier lifetime which can be depicted by [32]:

$$\tau_{N_{th}} = (\alpha + \beta N_{th} + \gamma N_{th}^2)^{-1}, \quad (13)$$

where α , β and γ express system recombination coefficients. Then, according to the cyclic power model, the power output formula from the transmitting end to the receiving end of the system can be obtained [28], [32]:

$$P_{beam} = \frac{2(1 - R_2)}{(1 + R_2)[\delta_t - \ln R_2]} (P_P - P_{th}), \quad (14)$$

where $P_P = \eta_P P_{in}$ expresses the input pump energy, P_{beam} is the external beam output from the reflector M2, and $\delta_t = 1 - T_{loss}R_1$ is introduced to define the energy loss caused by the

absorption, reflection, and refraction of the transmission medium, the diffraction loss and the overflow loss of the light beam when it is reflected by the end mirror M1. Furthermore, we can obtain the conversion efficiency of the P_{in} to P_{beam} :

$$\eta_b = \frac{2(1 - R_2)}{(1 + R_2)[\delta_t - \ln R_2]} \left(1 - \frac{P_{th}}{\eta_P P_{in}}\right), \quad (15)$$

where P_{in} is the input electric power and η_P is the conversion efficiency of the P_{in} to P_P which is a constant parameter based on the pump source.

E. Charging Power Output and Data Receiving

We get the external beam on the reflector M2 at the receiver. Then, we use a beam splitter to divide the external beam into two. One part will be transferred to the PV cell for power charging. The other part will be caught by the APD for data receiving.

1) *Energy harvesting*: This part of the external beam separated by the beam splitter is transmitted to the surface of the photovoltaic cell through a homogenizing waveguide. Then, the beam will be converted into electrical energy through photoelectric conversion, transmitted to the rectifier module, and used for device charging. This process can be expressed by the following formula [33]:

$$P_E = \mu P_{beam}, \quad (16)$$

$$P_{E_{out}} = a_1 P_E + b_1,$$

where μ expresses the power split ratio, P_E is the split laser energy used for electrical conversion. The parameter a_1 is the slope efficiency of photoelectric conversion, and b_1 is the threshold power of PV.

$$\eta_E = \frac{a_1 P_E + b_1}{P_{in}}. \quad (17)$$

2) *Data receiving*: The remaining part of the external beam separated by the beam splitter will act on the APD. The APD converts optical signal into an electrical signal while receiving the data. This process can be depicted as:

$$P_D = (1 - \mu) P_{beam}, \quad (18)$$

$$P_{D_{out}} = \nu P_D,$$

where ν is the optical-to-electrical conversion responsivity of APD.

When APD is receiving data, photoelectric conversion will produce thermal noise and shot noise. Among them, thermal noise can be expressed by the following formula [34]:

$$n_{\text{thermal}}^2 = \frac{4KT B_x}{R_L}, \quad (19)$$

where K is the boltzmann constant, T is the background temperature, and R_L is the load resistor. Moreover, the formula about the shot noise factor is [34]

$$n_{\text{shot}}^2 = 2q(P_{D_{out}} + I_{bg})B_x, \quad (20)$$

where q is the electron charge, B_x is the bandwidth, I_{bg} is the background current. At this point, the major noise of the communication module can be defined:

$$N_M^2 = n_{\text{shot}}^2 + n_{\text{thermal}}^2. \quad (21)$$

Finally, we can obtain spectral efficiency of the system as [35]:

$$\tilde{C} = \frac{1}{2} \log\left(1 + \frac{(P_{D_{out}})^2 e}{2\pi N_M^2}\right). \quad (22)$$

III. NUMERICAL EVALUATION

In this section, we will evaluate the proposed system by analyzing the transmission distance, beam radius, external beam power output, and channel capacity. Before the calculation, we set some constant parameters of the system whose corresponding values are listed in Table I.

A. Stable Transmission Distance

From the principle in Section II.C, it is known that for the beam to perform continuous reciprocating oscillation between the receiver and the transmitter, the cavity needs to be stable. A highly stable resonant cavity can effectively constrain the transmission of the resonant beam, which is the prerequisite for long-distance transmission of the resonant beam. In the RB system, since the TIM structure is introduced in this system, the influence of the telescope structure on the long-distance transmission stability of the cavity should be analyzed.

Figure. 6 presents the relationship of the system's maximum transmission distance and telescope adjustment parameters. It is worth noting that the maximum transmission distance D_{Max} here refers to the extreme value of d_2 when the stable cavity condition is satisfied. It is an ideal value which represents the system's transmission capability, in reality, the transmission distance of the system will be reduced by the energy attenuation such as air absorption. As is

TABLE I
PARAMETERS

| Parameter | Symbol | Value |
|---|------------------|---|
| TIM's position | d_1 | 10 mm |
| L1's focal length | f_1 | -5 mm |
| Resonant beam's wavelength | λ | 980 nm |
| Pump beam's wavelength | λ_{pump} | 808 nm |
| Pump source efficiency | η_P | 0.7 |
| Gain factor | g_0 | 2000 cm ⁻¹ |
| Transparency carrier density | N_0 | 1.7 * 10 ¹⁸ cm ⁻³ |
| Light quantum | E | 2.46 * 10 ⁻²² J |
| Longitudinal confinement factor | Γ | 2.0 |
| Round trip loss coefficient | T_{loss} | 0.99 |
| Pump area diameter | d_{pump} | 100 μ m |
| Quantum well thickness | L_w | 8 nm |
| Quantum well quantity | N_w | 14 |
| Monomolecular recombination coefficient | α | 10 ⁷ sec ⁻¹ |
| Bimolecular recombination coefficient | β | 10 ⁻¹⁰ cm ³ /sec |
| Auger recombination coefficient | γ | 10 ⁻³⁰ cm ⁶ /sec |
| Background temperature | T | 300 K |
| Boltzmann constant | K | 1.38 * 10 ⁻²³ J/K |
| APD's conversion responsivity | ν | 0.6 A/W |
| Noise bandwidth | B_x | 811.7 MHz |
| Background current | I_{bg} | 5100 ⁻⁶ A |
| Electronic charge | q | 1.6 * 10 ⁻¹⁹ C |
| Load resistance | R_L | 10 ³ Ω |

shown, the curve shows a downward trend with an increasing M. When M reaches a certain large value, the D_{Max} will become 0 and the system transmission is terminated. In addition, the transmission distance is affected by the curvature of the M2 mirror. When the M parameter is fixed, the greater the M2 curvature, the longer the effective transmission distance of the system. To present this influence brought by ρ_2 , we perform further numerical simulations and these results are presented in Fig. 7. The plot shows that ρ_2 and D_{Max} have a linear relationship. D_{Max} increases as ρ_2 increases. Numerically, D_{Max} is almost the same as ρ_2 . When M takes an appropriate value, the transmission distance of the system is capable of reaching 10 meters.

According to the above results and theories in Section II, it is known that the structure of the TIM will change the phase of the resonant beam, thereby distorting its propagation direction.

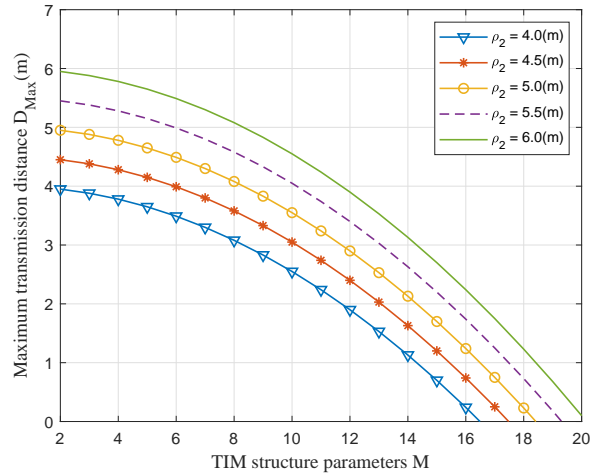


Fig. 6. Maximum transmission distance versus TIM structure parameter with different curvature values of the reflector M2

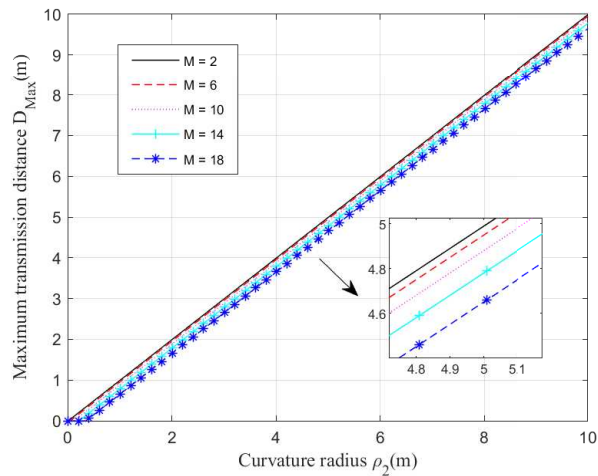


Fig. 7. Maximum transmission distance versus curvature of reflector M2 with different TIM structure parameter

Excessive telescope adjustment parameters will destroy the stability of the cavity. The output mirror will also feedback the amplitude of the incident light beam. The greater the curvature of the output mirror, the stronger the adjustment and convergence ability of the light beam, which is beneficial to the stability of the cavity during long-distance transmission.

B. Resonant Beam Radius on Gain Module

In order to suppress the transmission loss, the proposed system has a built-in TIM, which can compress the incident beam. To evaluate the compression performance, we analyze the spot

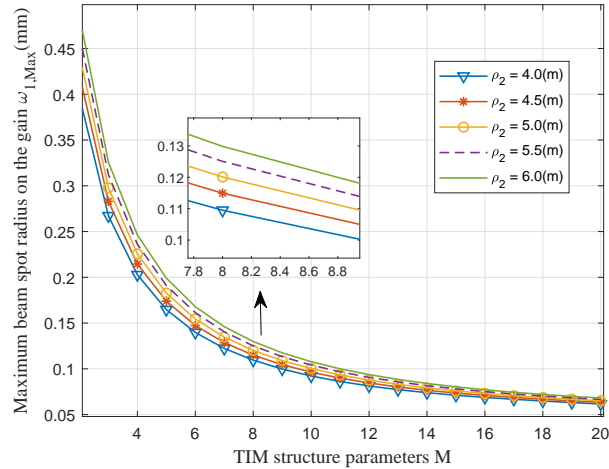


Fig. 8. Maximum beam radius on the gain versus TIM structure parameter for different curvature of reflector M2

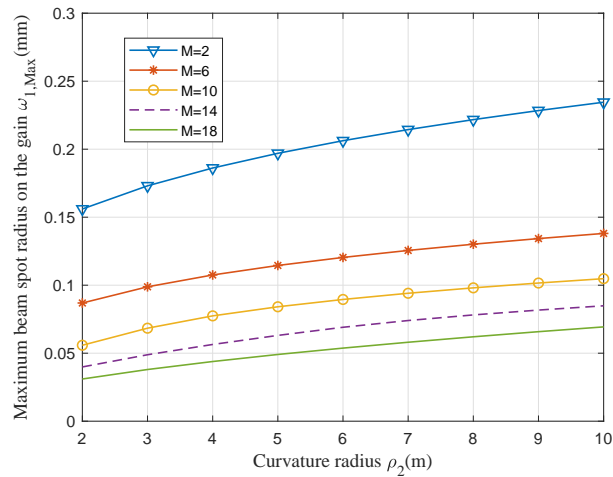


Fig. 9. Maximum beam radius on the gain versus curvature of reflector M2 with different TIM structure parameter

radius of the compressed beam on the gain. Fig. 8 depicts the relationship of the TIM structure parameter and the maximum beam spot radius. When the value of M parameter increases, the $\omega_{1,Max}$ shows a downward trend. Moreover, in the value range of 2 to 4, the beam radius decreases rapidly, and when the value is greater than 10, the decline of the beam spot tends to be gentle. What's more, the beam radius can be compressed from 0.45 mm to below 0.075 mm, which is 1/6 of the initial one. The result proves the beam compression ability of TIM, and the compression capacity will increase with the increase of the M parameter. However, this

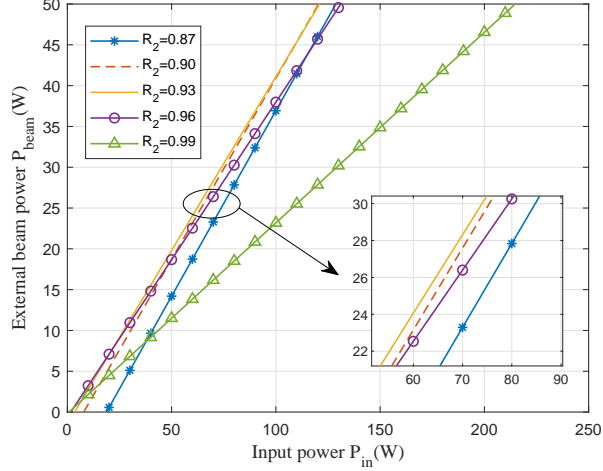


Fig. 10. External beam power versus input electric power for different reflectivity of reflector M2

compression capacity is limited. When the M parameter reaches a certain value, the compression capacity tends to be stable. Besides, the curvature of the mirror M2 will also affect the spot size. Fig. 9 shows the situation of curvature radius versus maximum beam spot radius on the gain. As is shown from the curves, $\omega_{1,Max}$ presents an upward trend with the increase of ρ_2 . What's more, the rising amplitude of the curve tends to be flat as the value of parameter M increases. However, the effect brought by ρ_2 is relatively small, specifically when the value of M is large.

According to the aforementioned analysis, preliminary conclusions can be obtained that the TIM can effectively compress the incident beam spot, which ensures that the resonant beam can effectively enter the micron-level size semiconductor gain without causing large diffraction loss. Combining the conclusions in Part A, the system can achieve long-distance and high beam compression at the same time by matching the M and ρ_2 reasonably.

C. External Beam Power Output

After the stable cavity condition of the system is established, with the energy accumulating, the energy will eventually emerge from reflector M2 in the form of the external laser beam. Then, the beam will enter the PV and APD respectively under the function of the beam splitter, realizing the electric power output and data reception. To evaluate the performance of the power output, we first calculate and analyze the power and energy conversion efficiency of the laser beam before entering the beam splitter. Then, we set the splitting ratio μ of the beam splitter

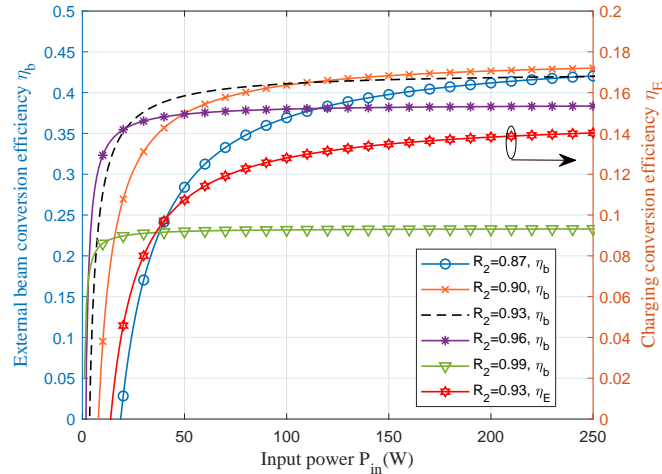


Fig. 11. Charging and external beam conversion efficiency as a function of input power for different M2's reflectivity

to 1, and analyze the total conversion efficiency of the system when it is only used for power charging, which can evaluate the efficiency improvement of the proposed system compared with the traditional system.

Figure. 10 describes the change of the beam output power on the reflector M2. As can be seen, the output beam power has a linear relationship with the input power. As the input power increases, the output beam power also increases. What's more, the threshold power is small. When the appropriate parameters are selected for R_2 , the threshold of the system is only a few watts. Besides, through simulating separately by changing the parameters of R_2 , we discover that the slope efficiency changes with the R_2 changing. When the reflectivity varies from 0.9 to 0.99, the slope efficiency presents an upward trend. To explore the impact of R_2 on the P_{beam} , we made a numerical simulation and presented it in Appendix A.

Figure. 11 presents the curves of energy conversion efficiency versus input power. The conversion efficiency performance with different R_2 shows a similar tendency. Overall, with P_{in} increase, η_b and η_E will rise rapidly and then stabilize. When R_2 takes an appropriate value, such as 0.87, 0.9 and 0.93, the beam power conversion efficiency η_b can reach 40% and close to 45%. Besides, similar to the output beam power, the reflectivity of the M2 also has a greater impact on the conversion efficiency. On the whole, a greater reflectivity will cause conversion efficiency to decrease. But this effect is not linear. We have further explored the influence of reflectivity, and this analysis of R_2 on the η_b is available in Appendix A. Furthermore, from the curve of η_E

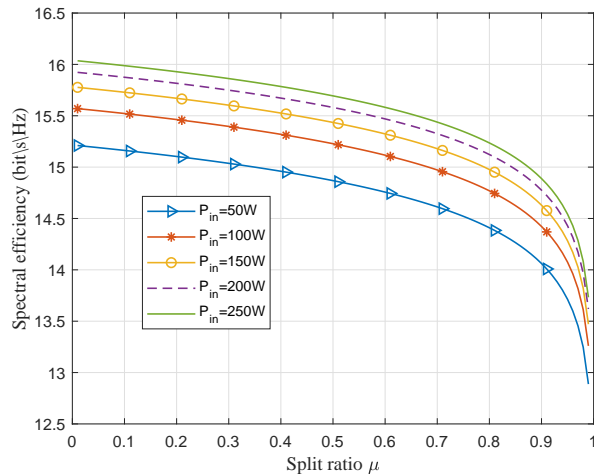


Fig. 12. Spectral efficiency versus power split ratio with different input power

($\mu=1$), the end-to-end conversion efficiency of the system is nearly 14% at the $P_{in}=210W$, while the efficiency of a normal system is just about 1% [11]. The end-to-end conversion efficiency of the proposed system is 14 times that of the traditional system.

According to the numerical results above, a brief summary can be obtained that the new structure we proposed in this paper, thanks to the TIM's spot compression and the high photon conversion of the semiconductor gain, can effectively improve the conversion efficiency of the system on the original basis.

D. Channel Capacity

After the function of beam splitter, part of the external beam will be caught by the APD for data receiving.

Figure. 12 depicts curves of split ratio versus spectral efficiency. The curve shows a downward trend with an increase of μ . The decline of the curve is relatively gentle at the beginning. When μ is greater than 0.8, \tilde{C} begins to drop sharply. What's more, a large input power will make the curve move upward, which causes the overall value of μ to become large. We further explore the change of the power efficiency from input power to beam power which is presented in Fig. 13. As can be seen, when the APD module receives the beam power, the spectral efficiency will fast rises to a larger value. Then, with the input power continues to increase, the spectral efficiency of the system increases slowly.

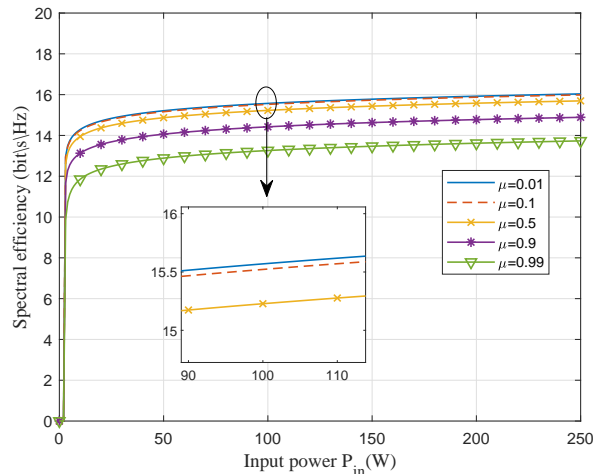


Fig. 13. Spectral efficiency versus input power for different power split ratio

According to the analysis in Section II, $1-\mu$ represents the proportion of external beam entering the APD, which means the larger μ , the less beam energy is allocated to the APD. Based on it and combining the above analysis, the spectral efficiency of the APD is affected by the amount of beam energy that enters. The greater the input beam energy, the higher the spectral efficiency of the APD. However, this influence is relatively small and limited. Taking $\mu = 0.01$ (most energy is split to APD) as an instance, when P_{in} increases from 50W to 250W, the spectral efficiency only increases 1 bit/s/Hz. In summary, through reasonable matching of splitting ratio and input power, the system's data transmission spectrum efficiency can reach up to 15 bit/s/Hz.

IV. CONCLUSIONS

In this paper, we proposed a high-efficiency resonant beam charging and communication system using the telescope internal modulator and the semiconductor gain medium. Relying on theories of transmission matrix, energy cycle, and channel capacity, we established an analytical model for the energy transfer efficiency and spectral efficiency of the proposed system. The numerical results illustrate that the system can realize long-range data and energy transfer. Compared with the traditional system with the solid-state gain medium without the telescope internal modulator, the energy conversion efficiency is increased by 14 times and the spectrum efficiency can be above 15 bit/s/Hz.

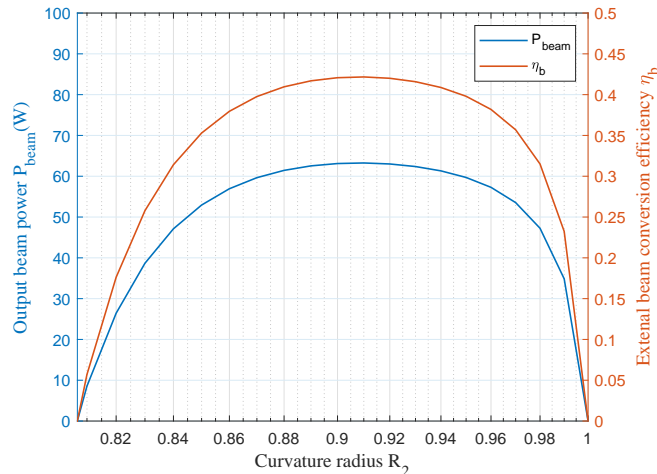


Fig. 14. M2's reflectivity versus external beam power and beam conversion efficiency

APPENDIX A

THE IMPACT OF THE M2'S REFLECTIVITY ON OUTPUT BEAM POWER AND CONVERSION EFFICIENCY

From Fig. 10 and 11, the performance of the beam power and conversion efficiency will be influenced by M2's reflectivity. To explore the influence of R_2 on these two parameters, we have carried out further calculations. Fig. 14 presents the curves of R_2 versus P_{beam} and η . It can be seen from the blue dotted line that, as the value of R_2 increases from 0.8 to 1, the power will first increase and then decrease, and the maximum value is 63 W when $R_2 \approx 0.9$. The solid red line shows the relationship between η_b and R_2 . The trend of the curve is the same as the power change curve. When R_2 takes nearly 0.9, the conversion efficiency can reach 0.43. From the curves, we can obtain the influence law of R_2 on P_{beam} and η_b , and obtain the optimal value of R_2 that satisfies the extreme performance of the system. It is worth noting that when R_2 is less than 0.8, there is no power output, which indicates that the loss of the system is greater than the gain at this time, and the energy channel cannot be established.

REFERENCES

- [1] M. Series, "IMT vision—framework and overall objectives of the future development of IMT for 2020 and beyond," *Recommendation ITU*, vol. 2083, 2015.
- [2] K. Jin and W. Zhou, "Wireless laser power transmission: a review of recent progress," *IEEE transactions on power electronics*, vol. 34, no. 4, pp. 3842–3859, 2018.

- [3] S. Y. R. Hui, W. Zhong, and C. K. Lee, "A critical review of recent progress in mid-range wireless power transfer," *IEEE Transactions on Power Electronics*, vol. 29, no. 9, pp. 4500–4511, 2013.
- [4] X. Lu, P. Wang, D. Niyato, D. I. Kim, and Z. Han, "Wireless charging technologies: Fundamentals, standards, and network applications," *IEEE Communications Surveys & Tutorials*, vol. 18, no. 2, pp. 1413–1452, 2015.
- [5] J. Lim, T. S. Khwaja, and J. Ha, "Wireless optical power transfer system by spatial wavelength division and distributed laser cavity resonance," *Opt. Express*, vol. 27, no. 12, pp. A924–A935, Jun 2019.
- [6] Y. Huang and B. Clerckx, "Waveform design for wireless power transfer with limited feedback," *IEEE Transactions on Wireless Communications*, vol. 17, no. 1, pp. 415–429, 2017.
- [7] B. Scrosati and J. Garche, "Lithium batteries: Status, prospects and future," *Journal of power sources*, vol. 195, no. 9, pp. 2419–2430, 2010.
- [8] N. Shinohara, *Wireless power transfer via radiowaves*. Wiley Online Library, 2014.
- [9] H. Haken, "Laser theory," in *Light and Matter Ic/Licht und Materie Ic*. Springer, 1970, pp. 1–304.
- [10] Q. Zhang, W. Fang, Q. Liu, J. Wu, P. Xia, and L. Yang, "Distributed laser charging: A wireless power transfer approach," *IEEE Internet of Things Journal*, vol. 5, no. 5, pp. 3853–3864, 2018.
- [11] W. Wang, Q. Zhang, H. Lin, M. Liu, X. Liang, and Q. Liu, "Wireless energy transmission channel modeling in resonant beam charging for IoT devices," *IEEE Internet of Things Journal*, vol. 6, no. 2, pp. 3976–3986, 2019.
- [12] M. Liu, H. Deng, Q. Liu, J. Zhou, M. Xiong, L. Yang, and G. B. Giannakis, "Simultaneous mobile information and power transfer by resonant beam," *IEEE Transactions on Signal Processing*, pp. 1–1, 2021.
- [13] M. A. Khalighi and M. Uysal, "Survey on free space optical communication: A communication theory perspective," *IEEE communications surveys & tutorials*, vol. 16, no. 4, pp. 2231–2258, 2014.
- [14] H. Li and Y. Huang, "The architecture of blind equalizer for MIMO free space optical communication system," in *Society of Photo-Optical Instrumentation Engineers (SPIE) Conference Series*, ser. Society of Photo-Optical Instrumentation Engineers (SPIE) Conference Series, vol. 10158, Oct. 2016, p. 101581H.
- [15] W. Fang, H. Deng, Q. Liu, M. Liu, Q. Jiang, L. Yang, and G. B. Giannakis, "Safety analysis of long-range and high-power wireless power transfer using resonant beam," *IEEE Transactions on Signal Processing*, 2021.
- [16] W. Chen, S. Zhao, Q. Shi, and R. Zhang, "Resonant beam charging-powered UAV-assisted sensing data collection," *IEEE Transactions on Vehicular Technology*, vol. 69, no. 1, pp. 1086–1090, 2019.
- [17] X. Liu, Y. Liu, Y. Chen, and L. Hanzo, "Trajectory design and power control for multi-UAV assisted wireless networks: A machine learning approach," *IEEE Transactions on Vehicular Technology*, vol. 68, no. 8, pp. 7957–7969, 2019.
- [18] M. Xiong, M. Liu, Q. Zhang, Q. Liu, J. Wu, and P. Xia, "TDMA in adaptive resonant beam charging for IoT devices," *IEEE Internet of Things Journal*, vol. 6, no. 1, pp. 867–877, 2018.
- [19] M. Xiong, Q. Liu, M. Liu, X. Wang, and H. Deng, "Resonant beam communications with photovoltaic receiver for optical data and power transfer," *IEEE Transactions on Communications*, vol. 68, no. 5, pp. 3033–3041, 2020.
- [20] M. S. Aziz, S. Ahmad, I. Husnain, A. Hassan, and U. Saleem, "Simulation and experimental investigation of the characteristics of a pv-harvester under different conditions," in *2014 International Conference on Energy Systems and Policies (ICESP)*. IEEE, 2014, pp. 1–8.
- [21] J. C. Campbell, "Recent advances in telecommunications avalanche photodiodes," *Journal of Lightwave Technology*, vol. 25, no. 1, pp. 109–121, 2007.
- [22] M. Born and E. Wolf, *Principles of optics: electromagnetic theory of propagation, interference and diffraction of light*. Elsevier, 2013.
- [23] R. N. N. Hodgson and I. H. Weber, *Laser Resonators and Beam Propagation*. Springer, 2005, vol. 108.
- [24] V. Magni, "Multielement stable resonators containing a variable lens," *JOSA A*, vol. 4, no. 10, pp. 1962–1969, 1987.

- [25] P. Baues, "Huygens' principle in inhomogeneous, isotropic media and a general integral equation applicable to optical resonators," *Opto-electronics*, vol. 1, no. 1, pp. 37–44, Feb. 1969.
- [26] H. Kogelnik, "Imaging of optical modes—resonators with internal lenses," *Bell System Technical Journal*, vol. 44, no. 3, pp. 455–494, Mar. 1965.
- [27] M. Eichhorn, *Laser physics: from principles to practical work in the lab*. Springer Science & Business Media, 2014.
- [28] W. Koechner, *Solid-state laser engineering*. Springer, 2013, vol. 1.
- [29] W. W. Chow, S. W. Koch, and M. I. Sargent, *Semiconductor-laser physics*. Springer Science & Business Media, 2012.
- [30] H. Soda, K. ichi Iga, C. Kitahara, and Y. Suematsu, "GaInAsP/InP surface emitting injection lasers," *Japanese Journal of Applied Physics*, vol. 18, no. 12, pp. 2329–2330, dec 1979.
- [31] H. Soda, Y. Motegi, and K. Iga, "Gainasp/inp surface emitting injection lasers with short cavity length," *IEEE Journal of Quantum Electronics*, vol. 19, no. 6, pp. 1035–1041, 1983.
- [32] M. Kuznetsov, F. Hakimi, R. Sprague, and A. Mooradian, "High-power (>0.5-W CW) diode-pumped vertical-external-cavity surface-emitting semiconductor lasers with circular TEM₀₀ beams," *IEEE Photonics Technology Letters*, vol. 9, no. 8, pp. 1063–1065, 1997.
- [33] Q. Zhang, W. Fang, M. Xiong, Q. Liu, J. Wu, and P. Xia, "Adaptive resonant beam charging for intelligent wireless power transfer," *IEEE Internet of Things Journal*, vol. 6, no. 1, pp. 1160–1172, 2018.
- [34] F. Xu, M. Khalighi, and S. Bourenane, "Impact of different noise sources on the performance of PIN- and APD-based FSO receivers," in *Proceedings of the 11th International Conference on Telecommunications*, Jun. 2011, pp. 211–218.
- [35] A. Lapidoth, S. M. Moser, and M. A. Wigger, "On the capacity of free-space optical intensity channels," *IEEE Transactions on Information Theory*, vol. 55, no. 10, pp. 4449–4461, 2009.